Fig. 3 Variation of density ratio across the shock with shock angle: ●, experimental data; ———, frozen predictions; and ×, equilibrium predictions.

predictions of thermodynamic parameters, and compared with similarly predicted upstream density, for a variety of shock angles.

The variation of the density ratio with shock angle is plotted in Fig. 3. As would be expected, density ratio tends to increase with increasing shock angle. The experimental data lie between the values predicted from ideal and equilibrium calculations. This supports the validity of the computed freestream conditions.

For the cylinder, the shock standoff distance normalized by the cylinder radius was measured to be 0.13. A correlation given by Hornung[7] for flow over blunt bodies was used to predict a standoff distance from the density jump across the shock. This value was calculated to he 0.47 for perfect gas conditions and 0.21 for equilibrium, both being significantly larger than that measured. A number of possible reasons for this have been considered. First, Hornung's correlation was developed for a dissociating nitrogen gas flow. The difference between correlations for nitrogen and air can he expected to he unimportant. However, the partially dissociated freestream and the presence of electrons behind the bow shock may influence the accuracy of the correlation in this case. Second, the assumption of two dimensionality may not be valid for the model used. Comparison of the cylinder dimensions (diameter 20 mm and length 25 mm) confirms that three-dimensional effects may be significant. Deviation from two dimensionality results in a curvature of the shock along the direction of the cylinder axis and a reduction in the standoff distance. Hornung's correlation for a cylinder would then overpredict the shock standoff distance. A third possibility is the influence of radiation cooling. At the high velocities existing in the flow, extremely high temperatures can be expected, at which radiative losses would lead to a lowering of the density and hence shock standoff distance. The importance of each of these effects on the shock standoff for the cylinder is to be the subject of future experimentation.

Conclusions

Good quality interferograms of superorbital air flow around a range of models have been recorded holographically. From the images, shock angles and standoff distances have been measured. The results for flow over the wedges gave density ratios that lie within expected limits. However, the shock standoff distance for the cylinder was found to be smaller than expected and a number of explanations have been proposed.

The results discussed here represent the initial measurements obtainable from holographic interferometry. Considerably more information about the density field around models is to be extracted by more detailed analysis of these results and extension to three-dimensional imaging.

References

[1]Neely, A. J., and Morgan, R. G., "The Superorbital Expansion Tube Concept, Experiment and Analysis," *Aeronautical Journal,* Vol. 98, *No.* 973, 1994, pp. 97–105.

[2]Tanner, L. H., "A Holographic Interferometer and Fringe Analyzer, and Their Use for the Study of Supersonic Flow," *Optics und Luser Technology,* Vol. 4, No. 6, 1972, pp. 281–287.

[3]Spring, W. C., Yanta, W. J., Gross, K., and Lopez, C. A., "The Use of Holographic Interferometry for Flow Field Diagnostics," *New Trends in Instrumentation for Hypersonic Research,* edited by A. Boutier, Kluwer Academic, Dordrecht, The Netherlands, 1993, pp. 97–112.

[4]Eitelberg, G., Fleck, B., and McIntyre, T. J., "Holographic Interferometry on the High Enthalpy Shock Tunnel in Gottingen," AGARD:ARW, 1992.

[5]Hornung, H. G., and Sandeman, R. J., "Interferometric Measurements of Radiating Ionizing Argon Flow over Blunt Bodies." *Journal of Physics D: Applied Physics,* Vol. 7, No. 6, 1974, pp. 920–935.

[6]Liepmann, H. W., and Roshko, A., *Elements of Gasdynamics,* Wiley, New York, 1957, p. 87.

[7]Hornung, H. G., "Non-equilibrium Dissociating Nitrogen Flow over Spheres and Circular Cylinders," *Journal of Fluid Mechanics, Vol.* 53, Pt. 1, 1972, pp. 149–176.

Accurate Numerical Integration of State–Space Models for Aeroelastic Systems with Free Play

Mark D. Conner,* Lawrence N. Virgin,'
and Earl H. Dowell[‡]
Duke University, Durham, North Carolina 27708-0300

Nomenclature

A_i	= state–space coefficient matrix for the ith linear subdomain
$a, c, r_\alpha, r_\beta, x_\alpha,$	= typical section parameters as defined in
$x_\beta, \mu, \omega_\alpha, \omega_\beta, \omega_h$	Ref. 2
b	= semichord
$f_n()$	= functional representation for the nth state
h_0	= initial plunge displacement
U	= freestream velocity
U_f	= linear flutter velocity
x_D	= additional dummy state variable used for Hcnon integration
x_n	= nth system state
a, β, h	= pitch, flap, and plunge displacements, respectively
$\zeta_\alpha, \zeta_\beta, \zeta_h$	= modal damping coefficients
$(\dot{\ })$	= velocity in the given degree of freedom

Introduction

THE general form of the equations of motion for the three-degree-of-freedom aeroelastic typical section in two-dimensional, incompressible flow was derived by Theodorsen.[1,2] Edwards et al.[3] proposed a state–space model for this linear system incorporating a two-state approximation to Theodorsen aerodynamics to determine the unsteady aerodynamic loads. However, similar state–space models for piecewise linear systems, such as those with free play in the structural stiffness of one or more degrees of freedom,

have typically not been exploited. Such systems are usually modeled in one of two ways: 1) using a describing function or harmonic balance approach to linearize the restoring force[4-7] or 2) using a much more complicated model requiring the solution of finite difference or vortex lattice equations in a time marching solution.[5,6 8] Recently, Lin and Cheng[4] have used a combination of linear state–space models to represent the distinct subdomains of a nonlinear aeroelastic system with free play. Their time-domain method incorporates Padé approximants for the determination of the unsteady loading on the airfoil. A key issue in using several distinct piecewise linear models to simulate the free-play system in the time domain is locating the exact point at which the system moves from one linear region into the next. Failure to capture this point accurately can result in a round-off error that may grow as the numerical integration proceeds and lead to numerical instability.[4] To avoid this type of instability, Lin and Cheng[4] employ a numerical algorithm with a self-adjusting time step to ensure that the system does not skip a subdomain as a point of discontinuity is approached. Once it is determined that the system has moved into another subdomain, the method of bisection is used to accurately determine the switching point. An alternative means of accurately and efficiently determining the switching point in the time domain is proposed in this Note.

Methodology

Adaptation of Henon's method for the computation of Poincaré maps allows for determination of the switching point in a piecewise linear system to a very high precision in just one integration step by rearranging the state–space equations.' Henon's method is used to integrate a system of equations onto a given surface of section or to a given value of a state variable. The technique involves interchanging the independent variable and the state variable of interest. As a result, the equations are altered, and time becomes a dependent variable. By integrating the altered (Henon) equations over a specified step in the chosen state variable, the time at which the system reaches the given surface is returned as a dependent variable along with the values of the other states on the surface. For control surface free play, the control surface displacement is the state variable that will determine the linear subdomain. The range of the free play is known, and the goal is to integrate the system to the exact values for the upper and lower free-play boundaries. The numerical algorithm for control surface free play is as follows.

1) Identify the current linear subdomain. Within this subdomain, the state–space equations are of the form

$$\frac{d}{dt}\begin{Bmatrix} x_1 \\ \vdots \\ x_N \\ ---\\ x_D \end{Bmatrix} = \begin{bmatrix} & & \vdots & \\ & A, & \vdots & 0 \\ & & \vdots & \\ --&--&--&-- \\ & 0 & \vdots & \frac{1}{x_D} \end{bmatrix}\begin{Bmatrix} x_1 \\ \vdots \\ x_N \\ ---\\ x_D \end{Bmatrix}$$

$$= \begin{Bmatrix} f_1(x_1, \ldots, x_N) \\ \vdots \\ f_N(x_1, \ldots, x_N) \\ ------------\\ f_D(x_D) \end{Bmatrix} \quad (1)$$

where the subscript i represents the particular linear subdomain and x_D is a dummy variable, which will be used in the Henon integration.

2) Using a constant time step Runge–Kutta algorithm (with an appropriately sized time step), integrate the equations of motion for the given subdomain forward in time until a change in the piecewise linear subdomain is detected.

3) The distance from the current control surface position to the boundary that has been crossed can be easily calculated. The equations of motion can be rearranged so that the control surface displacement becomes the independent variable, and time becomes a dependent variable along with the remaining state variables. This is done by dividing each of the state equations in Eq. (1) by f_n, where

n represents the equation associated with control surface displacement.

4) The altered (Henon) system can then be integrated in space from the current location to the boundary. The result of this integration step will be the time at which the system reaches the boundary point and the values of the remaining states at that point.

5) Using the state values from the Henon integration as the initial conditions, determine the new linear subdomain and integrate the original state equations forward in time until the next boundary is crossed.

The preceding algorithm specifies the use of a constant time step Runge–Kutta algorithm; however, the Henon integration could easily be incorporated into any constant or adaptive time step state–space integration scheme. The primary advantage of the Henon method is that it allows for the exact location of the switching point in one integration step. The algorithm is given for a system with control surface free play, but the technique can be applied to systems with free-play nonlinearities in multiple degrees of freedom. Since the original nonlinearity has been maintained, the full spectrum of nonlinear response is possible, including decaying oscillations, limit cycles, nonperiodic motion, chaos, and divergent flutter.

Results

Figure 1 shows the steady-state phase projection and control surface time series for a system with control surface free play. The dashed lines represent the boundaries of the free-play region. The sharp corners at the boundaries are a result of a significant change in the structural stiffness between the free-play region and the regions with a structural restoring moment, and this is the feature that we wish to capture accurately and efficiently.

Henon vs Brute Force

Figure 2 shows how standard Runge–Kutta combined with Henon's method and standard Runge–Kutta alone can give different solutions for the same set of initial conditions. Each figure is the result of integrating the given system with ± 1 deg of control surface free play from the same set of initial conditions using a typical time step (40 steps/cycle). Figures 2a and 2b show that for the given set of initial conditions [$U = 397$ in./s (0.56^*U_f); $h_0/b = 0.04$] the
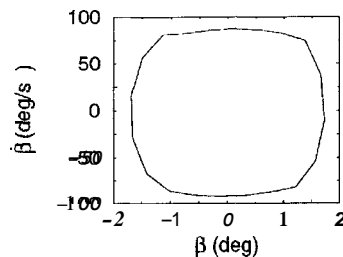

a)

b)
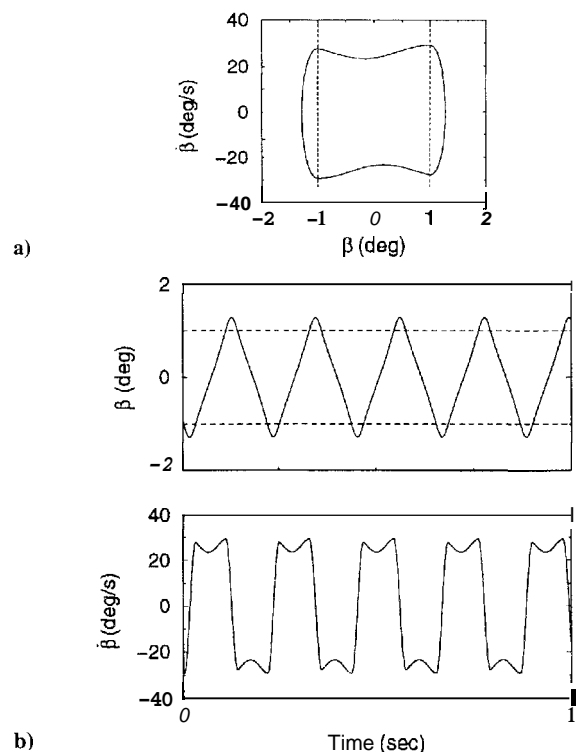
Fig. 1 For $U = 180$ in./s (0.25^*U_f); $h_0/b = 0.02$: a) control surface phase projection and b) time series for a system with a free-play region of ± 1 deg.
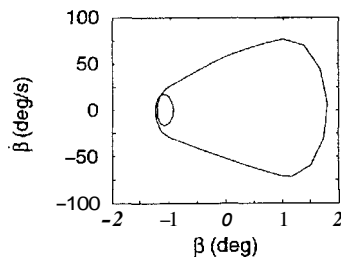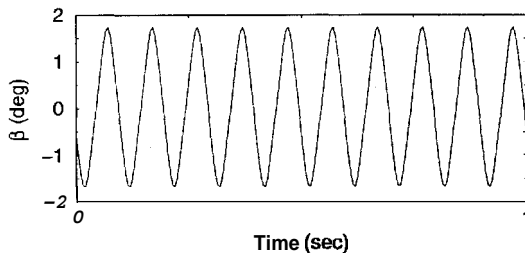
a) Phase projection Henon's method
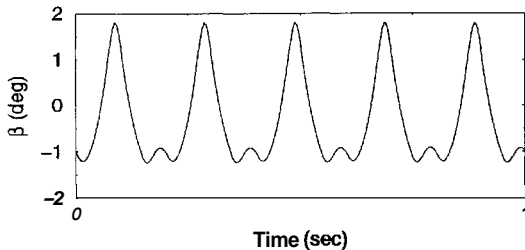
b) Displacement time series Henon's method

c) Phase projection standard Runge–Kutta

d) Displacement time series standard Rnnge–Kutta

Fig. 2   Control surface determined for $U = 397$ in./s (0.56^*U_f), $h_0/b = 0.04$ using 40 time steps per cycle and system parameters $a = -0.5$, $c = 0.5$, $\mu = 25.1$, r, $= 0.6827$, $rp = 0.09306$, $x_\alpha = 0.434$, $x_\beta = 0.0163$, $\omega_\alpha = 8.2$ Hz, $\omega_\beta = 18.4$ Hz, $\omega_h = 4.4$ Hz, $\zeta_\alpha = 0.024$, $\zeta_\beta = 0.0095$, and $\zeta_h = 0.017$ with Henon's method and standard Runge-Kutta.

control surface settles onto a periodic limit cycle using the algorithm described. Using standard Runge–Kutta integration with the same time step and simply changing subdomain equations at the first point after a boundary is crossed, the same system with the same set of initial conditions settles onto a coexisting periodic control surface motion, as shown in Figs. 2c and 2d. For the chosen system and parameter values, there are two competing limit cycle solutions, a feature commonly encountered in nonlinear systems. One of the solutions is the period 2 motion captured by the Henon integration. The other, found for much smaller initial plunge disturbances, is a periodic limit cycle, which is very similar to the solution found using the standard Runge–Kutta integration. In this case, the numerical error resulting from inaccurately identifying the switching point does not result in divergent behavior. The error does, however, cause the integration to settle onto an incorrect attractor. Nonlinear systems are generally quite sensitive to small changes. Boundaries that separate regions of different cyclic behavior may even be fractal.

Henon vs Bisection

Figure 2 shows that accurately locating the switching point is necessary for a robust numerical model. Several techniques including time step refinement and bisection[4] have been employed successfully to achieve this goal. Each of these techniques requires a number of additional numerical integration steps to locate the switching

Table 1   Numerical iterations to convergence

No. of significant figures	3	5	7	9	11	13
Avg. no. of bisection steps	3.6	9.5	16.4	23.4	29.7	35.4

point to a desired tolerance. In contrast, the Henon method requires only one additional integration step to locate the switching point to the accuracy of the input values for the boundaries of the free-play region. To determine the correlation between the desired tolerance for the switching point and the required number of integration steps using the method of bisection, the following calculations were made.

1) Using a standard Runge–Kutta algorithm, the system of equations was integrated forward in time from a given set of initial conditions until a boundary crossing was detected.

2) The method of bisection was then applied to the integration time step until the switching point was located to within a specified tolerance.

3) The number of steps required to reach the switching point from first crossing was recorded.

These steps were repeated for several initial conditions and two values for the initial integration step size (50 and 100 steps/cycle). The results were averaged and are given in Table 1. The tolerance is given in terms of the number of significant digits for the switching point relative to the given value for the free-play boundary. Note that all input and calculations involve double precision specifications. Therefore, the input value for the free-play boundaries is given to 16 significant digits. The Henon method achieves 16 significant digits of accuracy in one integration step.

A detailed report comparing numerical results based on Henon's method and experimental results for an aeroelastic typical section is being prepared for publication.'"

Conclusions

Results show the importance of accurately locating the switching point between linear subdomains when numerically integrating a piecewise linear system of equations. Henon's method locates the switching point to a high degree of accuracy in one integration step while eliminating the need for a specified tolerance. The benefits of the Henon algorithm would be even more evident when working with a chaotic system. To characterize chaotic systems, it is often necessary to simulate the system for thousands of cycles, since many descriptions are based on statistical properties. Use of Henon's method for piecewise linear chaotic systems will be far more efficient than standard integration techniques because the numerical error associated with locating the switching point is minimized while only requiring one additional integration step for each boundary crossing. Assuming that each of the techniques is based on the same standard Runge–Kutta algorithm, the error associated with the discretization for the numerical integration would be equivalent.

References

'Theodorsen, T., "General Theory of Aerodynamic Instability and the Mechanism of Flutter," NACA Rept. 496, 1935.

[2]Bisplinghoff, R. L., Ashley, H., and Halfman, R. L., *Aeroelasticity*, Addison–Wesley, Reading, MA, 1955.

[3]Edwards, J. W., Ashley, H., and Breakwell, J. V., "Unsteady Aerodynamic Modeling for Arbitrary Motions," *AIAA Journal*, Vol. 17, No. 4, 1979, pp. 365–374.

[4]Lin, W.-B., and Cheng, W.-H., "Nonlinear Flutter of Loaded Lifting Surfaces (I) & (II)," *Journal of the Chinese Society of Mechanical Engineers*, Vol. 14, No. 5, 1993, pp. 446–466.

'Price, S. J., Alighanbari, H., and Lee, B. H. K., "The Aeroelastic Response of a Two-Dimensional Airfoil with Bilinear and Cubic Structural Nonlinearities," *Journal of Fluids and Structures*, Vol. 9, 1995, pp. 175–193.

[6]Tang, D. M., and Dowell, E. H., "Flutter and Stall Response of a Helicopter Blade with Structural Nonlinearity," *Journal of Aircraft*, Vol. 29, No. 5, 1992, pp. 953–960.

[7]Yang, Z. C., and Zhao, L. C., "Analysis of Limit Cycle Flutter of an Airfoil in Incompressible Flow," *Journal of Sound and Vibration*, Vol. 123, No. 1, 1988, pp. 1–13.

[8]Kousen, K. A., and Bendiksen, O.O., "Limit Cycle Phenomena in Computational Transonic Aeroelasticity," *Journal of Aircraft*, Vol. 31, No. 6, 1994, pp. 1257–1263.

[9]Henon, M., "On the Numerical Computation of Poincaré Maps," *Physica D*, Vol. 5, 1982, pp. 412–414.

[10]Conner, M. D., Tang, D., Dowell, E. H., and Virgin, L. N., "Nonlinear Behavior of a Typical Airfoil Section with Control Surface Freeplay," *Journal of Fluids and Structures* (submitted for publication).

Deflection of Rectangular Orthotropic Plates Under Uniform Load

James A. August* and Shiv P. Joshi[†]
*University of Texas ut Arlington,
Arlington, Texas 76019-0018*

Introduction

IT has been analytically shown that the maximum deflection of rectangular orthotropic plates under uniform transverse loading with symmetric edge conditions does not occur at the center for all aspect ratios (AR).[1] Depending on the AR, curvatures for orthotropic plates under uniform loading have more than one maximum and reverse sign.

The purpose of this Note is to validate the aforementioned theoretical results. An experiment was performed to determine the deflected shape of symmetrically supported orthotropic plates under uniform load, as shown in Fig. 1. The experimental results were then compared with the mathematical model for shape and deflection. A symmetric clamped simply supported boundary condition case was selected, because it has a larger difference in peak to overall plate deflection compared with a plate that is simply supported on all sides.

Experimental Apparatus and Procedures

Fixture Fabrication

A fixture was designed to apply transverse uniform loading to a rectangular clamped simply supported plate, as shown in Fig. 2. The fixture consists of four clamp blocks and four knife edges that are bolted together to form two symmetric halves that are 15.24 cm (6.00 in.) wide. The knife edges on the upper half of the fixture are aligned with the clamp block faces to provide even boundary conditions without distorting the plate. The lower knife edges, which also form the sides of an air chamber, or bladder, are spaced approximately 1.3 mm (0.05 in.) from the plate to allow free rotation. During the experiment, the bladder was inflated with air to provide a uniform load on the lower plate surface. The fixture was designed to work with three different AR (1.88, 1.00, and 0.62) by changing the position of the clamp blocks. This required disassembly and realignment of the fixture for each AR tested.

After the fixture was assembled and aligned, the bladder was formed across the lower half of the fixture using an aluminum base plate on the bottom and a thin elastic sheet of nylon film on the tops of the lower knife edges. The nylon film was held in place with room
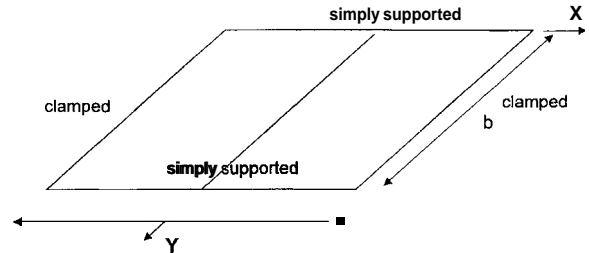

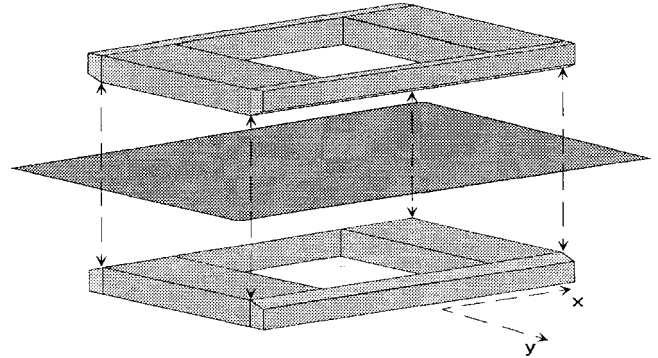Fig. 1   Coordinate system for plate analysis.

Fig. 2   Plate deflection text fixture.

temperature vulcanizing silicone adhesive, which was also used to seal the rest of the joints in the fixture. The final assembly of the fixture consisted of bolting the test plate between the upper and lower fixture halves.

Plate Fabrication

Graphite/epoxy was chosen for plate construction, because it was readily available and produces an orthotropic laminate having a significant ratio of maximum deflection to overall deflection variation for this experiment. The plate was fabricated from 16 plies of Hercules AS-4/3501-6 graphite/epoxy prepreg, which was laid up and autoclave cured as recommended by the manufacturer. This resulted in a finished plate that was 1.83 mm (0.072 in.) thick.

Experimental Setup

The fixture was set up on the bed of a large vertical milling machine, which provided the accuracy and repeatability necessary to make consistent deflection measurements. A dial indicator was mounted to the head of the milling machine in a manner that allowed the indicator tip to contact the plate through the complete deflection range. After aligning the test fixture with the dial indicator, the bed of the milling machine was set up to track the y axis across the center of the plate, because this is where the greatest amount of deflection was expected. A set of zero load deflection measurements was taken in 2.54-mm (0.10-in.) increments across the width of the plate. This resulted in 58 measurements because of interference between the fixture edge and the indicator tip. Subsequent measurements were then taken with various amounts of pressure applied to the fixture to load the plate. Pressure was supplied by a precision air pump or regulated shop air line and was recorded during each test using gauges that were calibrated with a U-tube mercury manometer.

Numerical Analysis

The deflection $w(x, y)$, given by a Levy solution for a plate whose sides at $x = \pm a/2$ is

$$w_p(y) + \frac{b^4}{D_2\pi^4} \sum_{n=1}^{\infty} \frac{a_n}{n^4} \left[\frac{s_2 \cosh(n\pi s_1 x/b) \sinh(n\pi s_2 c/2) - s_1 \cosh(n\pi s_2 x/b) \sinh(n\pi s_1 c/2)}{s_1 \cosh(n\pi s_2 c/2) \sinh(n\pi s_1 c/2) - s_2 \cosh(n\pi s_1 c/2) \sinh(n\pi s_2 c/2)} \right] \sin\left(\frac{n\pi y}{b}\right)$$